RSC Advances

ROYAL SOCIETY OF CHEMISTRY

www.rsc.org/advances

Cite this: DOI: 10.1039/c0xx00000x

www.rsc.org/xxxxxx

ARTICLE TYPE

Self-sacrifice template formation of ultrathin single-crystalline $ZnMn_2O_4$ nanoplates with enhanced Li-storage behaviors for Li-ion batteries

Siqi Zhu,‡ Yaoyao Shi,‡ Qiuli Chen, Zhiyi Chen, Ruiqi Bao, Chao Yang, Linrui Hou*, Gang Pang, and Changzhou Yuan*

Received (in XXX, XXX) Xth XXXXXXXXX 20XX, Accepted Xth XXXXXXXXX 20XX
DOI: 10.1039/b000000x

Ultrathin single-crystalline $ZnMn_2O_4$ nanoplates were first designed and tailored as an alternative anode for advanced Li-ion batteries *via* efficient self-sacrifice template synthetic strategy, and delivered large reversible capacity and desirable stability at high C rates

The ever-growing demands for advanced Li-ion batteries (LIBs) with large mass/volume capacity and desirable cycling durability have greatly stimulated tremendous research interests in exploring high-performance electrode materials.[1] Thus, various 3*d* transition-metal oxides (TMOs) have been investigated extensively, and received increasing attention as promising substitutes for commercial graphite-based anodes, benefiting from their safety, high specific capacity and natural abundance.[1] Interestingly enough, it has recently been established well as a smart strategy *via* elegant combination of two TMOs, or a TMO and one post-TMO, in typical spinel structure, to purposefully design appealing mixed anodes with remarkable electrochemical performance, benefiting from these complex chemical compositions and intriguing synergetic effects of their multi-functionalities.[2]

Among those mixed TMOs, binary manganites (AMn_2O_4, A = Zn, Co, Ni, *etc.*) of transition and/or post-transition metals are practically attractive anodes for LIBs in view of considerable advantages, such as, environmental friendliness, cost efficiency, abundance on earth, low lithium extraction voltage, and so on.[3] Especially, cubic spinel $ZnMn_2O_4$ (ZMO), where bivalent Zn(II) occupies the tetrahedral sites and trivalent Mn^{3+} inhabits the octahedral sites (**Fig. S1**, Electronic Supporting Information, ESI†), stands out from the AMn_2O_4 series as more promising and competitive anode. The ZMO can store Li^+ through not only the conversion reaction but the alloying mechanism between Zn and Li, rendering a high theoretical capacity of ~784 mAh g^{-1}.[4-9] Furthermore, the ZMO with environment-friendly Zn and Mn species ensures a higher energy density of a ZMO (anode)-based full batteries, thanks to low oxidation potentials (~1.2 – ~1.5 V) observed for manganese and zinc oxides.[3] In the past decade, various ZMO nano-architectures, including nanotubes,[4] nanowires,[5] nanofibers,[6] nanoparticles,[7, 8] and nanorods,[9] have thereby been extensively pursued to improve electrochemical Li-storage behaviors, owing to appealing merits from the nano-scaling and nano-engineering strategies.[10] To the best of our knowledge, scarce investigations of ultrathin ZMO nanoplates (NPs) can be retrieved as anode candidate for advanced LIBs, where decreased Li^+ diffusion, large electroactive sur-/interfaces, excellent accommodation of strain during Li^+ insertion/removal and short path length for electronic transport are guaranteed.[10] As a result, superior electrochemical Li-storage performance can be highly anticipated. Additionally, the crystallinity of the sample also has considerable influence upon the ultimate performance of the electrode material, and samples with poor crystallinity are not suitable for high-capacity applications, as established before.[7, 11]

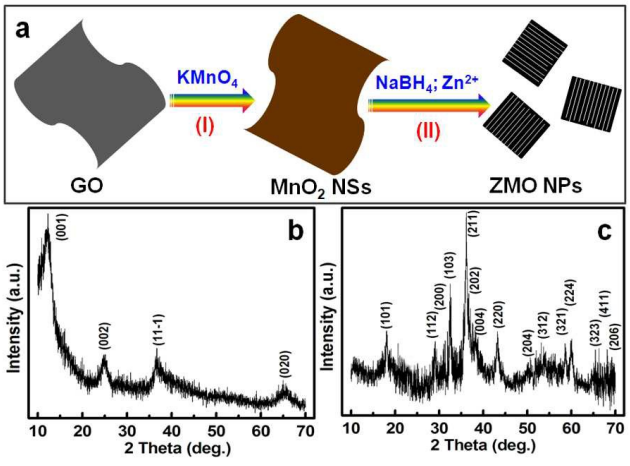

Fig. 1 (a) Schematic illustration for the self-sacrifice template synthesis, and wide-angle XRD patterns of the resulting ultrathin (b) MnO_2 NSs and (c) ZMO NPs

Based on the comprehensive consideration above, in the communication, we successfully established a facile yet efficient self-sacrifice template synthetic platform for fabricating ultrathin single-crystalline ZMO NPs. When further utilized as an intriguing anode for high-performance LIBs, the as-synthesized ZMO NPs remarkably exhibited large reversible capacity, and long-term electrochemical stability at high C rates.

As systematically presented in the experimental details (see ESI†), herein, two step self-sacrifice template synthetic methodology was efficiently developed to prepare ultrathin ZMO NPs, which is schematically illustrated in **Fig. 1a**. Clearly, two-dimensional (2D) MnO_2 nanosheets (NSs) were first *in situ* prepared by using 2D graphene oxide (GO) NSs[12] (**Fig. S**2, ESI†) as a template *via* a gradual redox process ($3C + 4\ MnO_4^- \rightarrow 4\ MnO_2 + CO_3^{2-} + 2HCO_3^-$)[13] between carbon atoms on the GO framework and MnO_4^- during hydrothermal process. Typical powder X-ray diffraction (XRD) pattern of the as-obtained MnO_2 specimen is shown in **Fig. 1b**. The four diffraction peaks at 2θ = 12.4 º, 24.9 º, 37.0 º, and 65.5 º are indexed well as the (001), (002), (11-1) and (020) planes, respectively, which confirms the formation of birnessite MnO_2 (JCPDS, #43-1456) without other crystalline phases. Then, chemical reduction of the resultant MnO_2 NSs was performed by using the reductant of BH_4^- at room temperature (RT) with the presence of Zn(II) to realize the phase transition from the $Mn(IV)O_2$ to spinel $ZnMn(III)_2O_4$.[8, 14, 15] Corresponding XRD characterization, as depicted in **Fig. 1c**, indicates that the final product can be successfully assigned to the tetragonal ZMO (JCPDS, #24-1133, space group:$I4_1/amd$, $a = b = 5.720$ Å, $c = 9.245$ Å, $\alpha = \beta = \gamma = 90$ °). Furthermore, as observed in Fourier transform infrared (FT-IR) spectrum (**Fig. S**3, ESI†) for the ZMO NPs, the peak at ~466 cm^{-1} can be related to the Zn-O stretching, and other peaks at ~507, ~621, and ~672 cm^{-1} arise from the Mn-O contributions, confirming the formation of ZMO phase.[16]

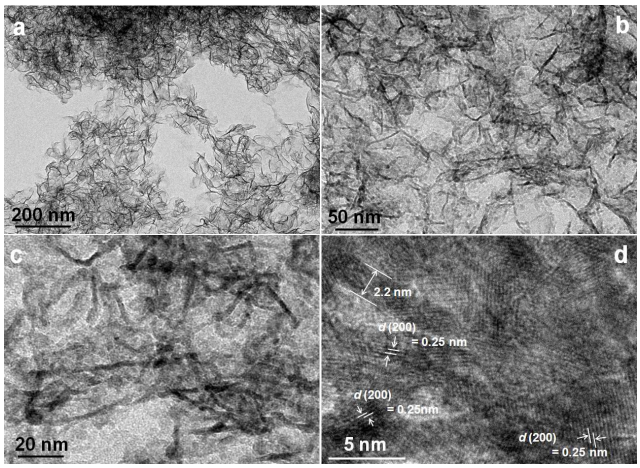

Fig. 2 (a-c) TEM and (d) HRTEM images of the 2D MnO_2 NSs

Fig. 2a-c demonstrate the representative transmission electron microscopy (TEM) images of the as-obtained MnO_2 NSs. Apparently, a large scale of 2D graphene-structure NSs with rippled silk morphology are evident, revealing the ultrathin feature of the MnO_2 NSs. It is due to the even larger lateral size than the thickness that the bending, curling and crumpling morphology is clearly presented. The dark strips are generally the folded edges and/or wrinkles of the NSs. The thickness of the 2D NSs is estimated as ~1.1 nm, as evaluated from the high-resolution TEM (HRTEM) image in **Fig. 2d**, which suggests that the MnO_2 NSs should be just composed of several layers of the MnO_2 atomic sheets. Furthermore, clear lattice fringes with a spacing of ~0.25 nm, corresponding to the (200) plane of the MnO_2, can be observed, verifying the well-crystalline nature of the NSs. This examination strongly confirms the excellent inheritance of resulting 2D MnO_2 NSs from the original GO template.

Fig. 3a displays the TEM images of the resultant ZMO NPs. Numerous nano-scaled particles with ~10 nm in size are obviously presented. Typical TEM energy dispersive spectrometer (EDS) elemental mapping analysis (**Fig. 3b**) evidently reveals the extremely homogeneous co-existence and uniform distribution of the Zn, Mn, and O elements in the product. Corresponding EDS data (**Fig. S4**, ESI†) collects chemical composition of the sample, showing the Mn/Zn atomic ratio of ~1/2, which is close to the stoichiometric ratio of the ZMO phase. As seen in **Fig. 3c**, nanoplate-like configuration with the transparent feature is evident, strongly verifying the ultrathin nature of the ZMO product, which further can be supported well by the HRTEM images (**Fig. 3d-e**). Furthermore, all these discernable lattice fringes in each NP present single orientation, as inspected in **Fig. 3d-e**, which strongly corroborates the single-crystalline characteristics of these NPs. Corresponding fast Fourier transformation (FFT) electron diffraction (ED) pattern (the inset in **Fig. 3d**) with clear diffraction spots further demonstrates the high orientation of these single-crystalline ZMO NPs.

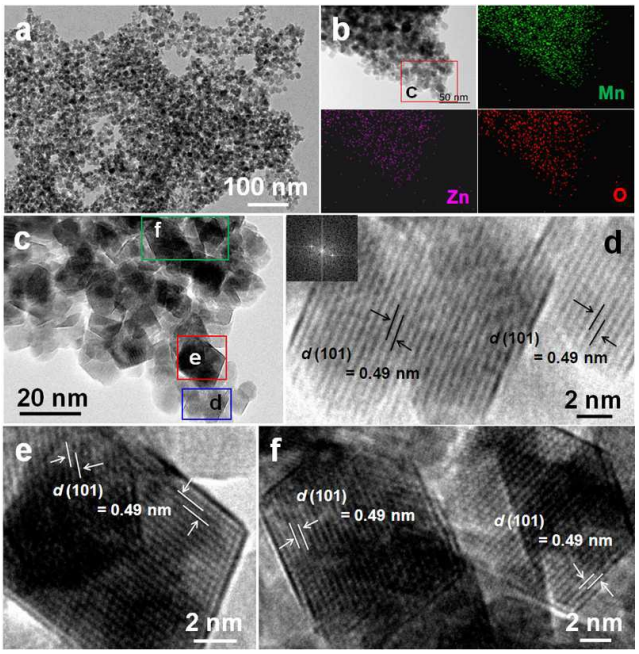

Fig. 3 (a) TEM image, (b) elemental (Mn, Zn, O) mapping images acted on the upper-left TEM image. The image in (c) is taken from the red rectangle region in the panel (b). The HRTEM images in (d), (e) and (f) are the magnified ones of the red, blue and green rectangle regions in panel (c), respectively. The inset in panel (d) is the corresponding FFT ED pattern generated from the panel

We next evaluate the electrochemical Li-storage performance of the resultant ZMO NPs as an anode for LIBs. **Fig. 4a** shows the typical cyclic voltammograms (CVs) for the initial three cycles at a sweep rate of 0.5 mV s^{-1} in the potential window of 0.01 – 3.0 V (*vs.* Li/Li^+). Consistent with other reports for ZMO anodes in literatures, a broad peak at approximately 1.1 V is discerned in the first cathodic scanning,

which is generally ascribed to the reduction of the Mn(III) to Mn(II), and the irreversible formation of the solid electrolyte interphase (SEI) layers.[4, 7, 9] One more strong cathodic peak sitting at ~0.25 V generally corresponds to the reduction of ZMO into Zn^0 and Mn^0 embedded in amorphous Li_2O matrix, and the further reaction of newly formed Zn with Li to yield the Li-Zn alloy. In the first anodic charging process, two broad peaks at ~1.21 and ~1.57 V can be attributed to the oxidation of Mn^0/Zn^0 to Mn^{2+}/Zn^{2+}, along with the decomposition of the Li_2O. The CV profile of the first cycle presented here is distinct greatly from the subsequent cycles, suggesting the wholly different Li-storage mechanism involved in the 1st cycle form the following ones. Note that two pairs of obvious redox peaks are observed in the CV profile from the 2nd cycle onward. Specifically, the one at ~0.51/~1.2 V (*vs.* Li/Li^+) is ascribed to the reduction/oxidation of the Mn(II)O, and the other located at ~0.8/~1.58 V (*vs.* Li/Li^+) in the CV curves is related to the reduction/oxidation of the Zn(II)O. Particularly, the CV curves of the 2nd and 3rd cycles almost overlap, confirming high reversibility and good structural durability of the ZMO NPs anode during the following Li^+ insertion/ extraction processes.

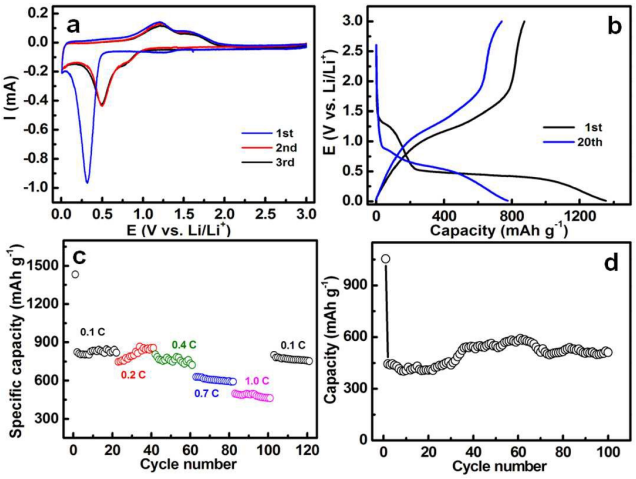

Fig. 4 Electrochemical evaluation of the ZMO NPs: (a) CVs of the initial three cycles; (b) charge-discharge plots at 0.5 C rate; (c) specific capacity over cycling at various rates; (d) cyclability at a high rate of 1.0 C

Fig. 4b depicts the galvanostatic charge/discharge plots of the ZMO NPs for the 1st and 20th cycles with 0.5 C rate (1 C = 784 mAh g^{-1}) over a cut-off potential range of 0.01 – 3.00 V (*vs.* Li/Li^+). As seen in the voltage-capacity profiles, the 1st discharge capacity is delivered as ~1353 mAh g^{-1}, corresponding to ~11.9 molar of Li^+ per mole ZMO, larger than the theoretical value of 1008 mAh g^{-1} (9 M of Li^+ per ZMO) resulting from three electrochemical processes (*i.e.* Li^+ intercalation, conversion reaction and alloy reaction) involved in the first one.[4-9] The extra capacity of ~345 mAh g^{-1} observed here should be rationally attributed to the formation of SEI layer at ultrathin ZMO NP anode/electrolyte interface. The first charge (*i.e.*, de-lithiation) plot demonstrates a stead and smooth voltage increase from 0.01 to 3.00 V, and the overall charging capacity is estimated as ~876 mAh g^{-1} (~7.7 molar of Li^+ per ZMO formula). An initial irreversible capacity loss of ~477 mAh g^{-1}, that is, the Coulombic efficiency (CE) of ~64.7% is estimated accordingly, which is even higher than other ZMO-based anodes, such as, ZMO nanorods (~61.8),[9] nanoflowers (~56.5%),[17] nanotubes (~58 – ~60%),[4] nanocrystals (~58 – ~63%),[7, 18] porous spheres (~56 – ~63%),[19] and so on. After 20 cycles, the discharge/charge profiles demonstrate qualitative resemblance to those for the 1st cycle except for the low capacities. Strikingly, the discharge and charge capacities still maintains as large as ~775 and ~741 mAh g^{-1}, respectively, corresponding to a high CE of ~96%. Besides large reversible capacity, high-rate performance is of great significance, especially for high-power devices. **Fig. 4c** illustrates the corresponding rate capacities of the ZMO NPs at 0.1 C, 0.2 C, 0.4 C, 0.7 C and 1.0 C, respectively. Obviously, after initial 22 cycles at a low rate of 0.1 C, the discharge capacity is gradually down to ~819 mAh g^{-1}, and afterwards, the average specific capacities are stably maintained as ~810, ~761 and ~607 mAh g^{-1} at the current rates of 0.2 C, 0.4 C and 0.7 C, respectively. More appealingly, when the rate is up to 1.0 C rate, the ZMO NPs still deliver a high average capacity of ~482 mAh g^{-1}, much higher than that of the commercially available graphite-based anodes (~372 mAh g^{-1}).[4] When the rate suddenly turns back to 0.1 C, the stable capacity of around 776 mAh g^{-1} still can be retrieved once more, revealing its good rate behaviour, which is of great importance to its practical applications for high-power LIBs as a promising anode.

Long-term cycling stability particularly at high rates is additionally critical requirement for practical LIBs application. **Fig. 4d** shows the capacity variation as a function of cycle number at 1.0 C rate for up to 100 cycles. Notably, the discharge capacity first decreases during the first ~10 cycles. The discharge capacity then exhibits a relatively stable cycling performance, and maintains at ~410 mAh g^{-1}. Interestingly, after cycling for ~20 cycles, the capacity begins to gradually grow again. Such phenomenon is commonly observed for TMOs-based anodes, and generally related to the reversible formation of a polymeric gel-like film originating from kinetic activation in the electrode.[20] More impressively, after cycling for 100 cycles, the ZMO NPs electrode still can obtain a discharge capacity of ~510 mAh g^{-1}, which is comparable to, and even better than other ZMO-based anodes.[4, 8, 9, 21]

In summary, we have successfully developed a two-step self-sacrifice template synthetic methodology to efficiently prepare ultrathin ZMO NPs, and further utilized it as a high-performance anode for LIBs. The intriguing ultrathin, well crystalline, and nano-scaled feature provide a short pathway for rapid Li^+/electron diffusion, and a large electrode/electrolyte contact area for Li^+ migration across the sur-/interfaces. Benefiting from these appealing structural merits, the as-fabricated ZMO NPs promised large reversible capacities and stable cycling performance at high C rates. More importantly, an efficient avenue is now open for future development of other potential electroactive AMn_2O_4 (A = Co, Ni, Cu, *etc.*) anodes for next-generation LIBs.

This work was supported by the National Natural Science Foundation of China (no. 51202004, 51572005, 51502003),

Anhui Province Funds for Distinguished Young Scientists (no. 1508085J09), and the Natural Science Foundation of Anhui Province (no. 1508085ME106).

Notes and references

School of Materials Science and Engineering, Anhui University of Technology, Ma'anshan, 243002, P. R. China
Email: houlr629@163.com; ayuancz@163.com

† Electronic Supplementary Information (ESI) available: The detailed synthesis conditions, crystallographic structure, XRD, FT-IR and EDS data. See DOI: 10.1039/b000000x/

‡ Theses authors contributed equally to this work

1 P. Poizot, S. Laruelle, S. Grugeon, L. Dupont and J. M. Tarascon, *Nature,* 2000, **407**, 496; L. Zhang, H. B. Wu and X. W. Lou, *Adv. Energy Mater.*, 2014, **4**, 1300958.

2 C. Z. Yuan, H. B. Wu, Y. Xie and X. W. Lou, *Angew. Chem. Int. Ed.*, 2014, **53**, 1488.

3 F. M. Courtel, H. Duncan, Y. Abu-Lebdeh and I. J. Davidson, *J. Mater. Chem.*, 2011, **21**, 11987; Z. C. Bai, Y. H. Zhang, Y. W. Zhang, C. L. Guo, B. Tang and D. Sun, *J. Mater. Chen. A* 2015, **3**, 5266; Z. C. Bai, N. Fan, Z. C. Ju, C. L. Guo, Y. T. Qian, B. Tang and S. L. Xiong, *J. Mater. Chem. A*, 2013, **1**, 10985.

4 J. G. Kim, S. H. Lee, Y. M. Kim and W. B. Kim, *ACS Appl. Mater. Interfaces*, 2013, **5**, 11321; L. H. Zhang, S. Q., Zhu, H. Cao, L. R. Hou and C. Z. Yuan, *Eur.-Chem. J.*, 2015, **21**, 10771.

5 S. W. Kim, H. W. Lee, P. Muralidharan, D. H. Seo, W. S. Yoon, D. K. Kim and K. Kang, *Nano Res.*, 2011, **4**, 505; Y. H. Zhang, Y. W. Zhang, C. L. Guo, B. Tang, X. M. Wang and Z. C. Bai, *Electrochim. Acta*, 2015, **182**, 1140.

6 L. Luo, H. Qiao, K. Chen, Y. Q. Fei and Q. F. Wu, *Electrochim. Acta*, 2015, **177**, 283.

7 Y. F. Deng, S. D. Tang, Q. M. Shi, L. T. Zhang, S. Z. Zhang and G. H. Chen, *J. Mater. Chem.*, 2011, **21**, 11987.

8 C. Z. Yuan, L. H. Zhang, L. R. Hou, L. Zhou, G. Pang and L. Lian, *Eur.-Chem. J.*, 2015, **21**, 1262.

9 Z. M. Zheng, Y. L. Cheng, X. B. Yan, R. T. Wang and P. Zhang, *J. Mater. Chem. A*, 2014, **2**, 149; Z. C. Bai, N. Fan, C. H. Sun, Z. C. Ju, C. L. Guo, J. Yang and Y. T. Qian, *Nanoscale*, 2013, **5**, 2442.

10 A. S. Aricò, P. Bruce, B. Scrosati, J. M. Tarascon and W. V. Schalkwijk, *Nat. Mater.*, 2005, **4**, 366; A. Manthiram, A. Vadivel Murugan, A. Sarkar and T. Muraliganth, *Energy Environ. Sci.*, 2008, **1**, 621.

11 C. M. Doherty, R. A. Caruso, B. M. Smarsly and C. J. Drummond, *Chem. Mater.*, 2009, **21**, 2895.

12 C. Z. Yuan, L. Yang, L. R. Hou, J. Y. Li, Y. X. Sun, X. G. Zhang, L. F. Shen, X. J. Lu, S. L. Xiong and X. W. Lou, *Adv. Funct. Mater.*, 2012, **22**, 2560; C. Z. Yuan, L. H. Zhang, L. R. Hou, G. Pang and W. C. Oh, *RSC Adv.*, 2014, **4**, 14408.

13 C. Z. Yuan, L. H. Zhang, H. Cao, S. Q. Zhu, J. D. Lin and L. R. Hou, *Nanotechnology*, 2015, **26**, 145401.

14 G. X. Zhao, J. X. Li, L. Jiang, H. L. Dong, X. K. Wang and W. P. Hu, *Chem. Sci.*, 2012, **3**, 433.

15 F. Y. Chen, J. Shen, B. Peng, Y. D. Pan, Z. L. Tao and J. Chen, *Nat. Chem.*, 2011, **3**, 79.

16 L. W. Zhang, H. Y. Cheng, R. L. Zong and Y. F. Zhu, *J. Phys. Chem. C*, 2009, **113**, 2368; P. K. Sharma and M. S. Whittingham, *Mater. Lett.*, 2001, **48**, 319.

17 L. F. Xiao, Y. Y. Yang, J. Yin, Q. Li, L. Z. Zhang, *J. Power Sources*, 2009, **194**, 1089.

18 Y. Y. Yang, Y. Q. Zhao, L. F. Xiao and L. Z. Zhang, *Electrochim. Acta*, 2008, **10**, 1117.

19 L. Zhou, H. B. Wu, T. Zhu and X. W. Lou, *J. Mater. Chem.*, 2012, **22**, 827; N. N. Wang, X. J. Ma, H. Y. Xu, L. Chen, J. Yue, F. E. Niu, J. Yang and Y. T. Qian, *Nano Energy*, 2014, **6**, 193; C. Z. Yuan, J. Y. Li, L. R. Hou, L. H. Zhang and X. G. Zhang, *Part. Part. Syst. Charact.*, 2014, **31**, 657.

20 J. Cabana, L. Monconduit, D. Larcher and M. R. Palacín., *Adv. Mater.*, 2010, **22**, E170; Y. R. Liu, J. Bai, X. J. Ma, J. F. Li and S. L. Xiong, *J. Mater. Chem. A*, 2014, **2**, 14236.

21 S. H. Choi and Y. C. Kang, *Int. J. Electrochem. Sci.*, 2013, **8**, 6281 G. Q. Zhang, L. Yu, H. B. Wu, H. E. Hoster and X. W. Lou, *Adv. Mater.*, 2012, **24**, 4609.

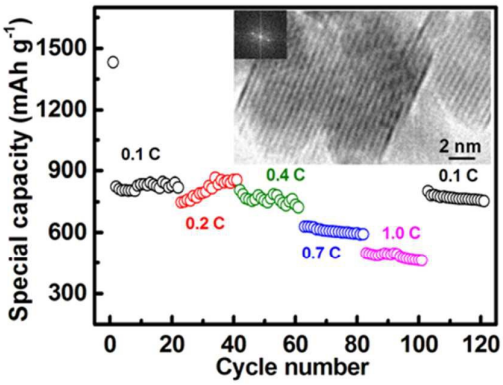

Ultrathin single-crystalline $ZnMn_2O_4$ nanoplates were first designed and tailored as anode for advanced Li-ion batteries *via* efficient self-sacrifice template synthetic strategy, and delivered excellent Li-storage performance at high C rates